doi:10.1093/mnras/sty2208



Downloaded from https://academic.oup.com/mnras/article-abstract/480/4/4912/5075590 by University of Illinois Law Library user on 01 April 2019

Dramatic X-ray spectral variability of a Compton-thick type-1 QSO at $z \sim 1$

T. Simm , ^{1*} J. Buchner , ^{2,3} A. Merloni, ^{1*} K. Nandra, ¹ Y. Shen, ⁴ T. Erben, ⁵ A. L. Coil, ⁶ C. N. A. Willmer and D. P. Schneider , ^{8,9}

Accepted 2018 August 10. Received 2018 August 8; in original form 2018 March 12

ABSTRACT

We report on the discovery of a dramatic X-ray spectral variability event observed in a $z\sim 1$ broad line type-1 QSO. The *XMM-Newton* spectrum from the year 2000 is characterized by an unobscured power-law spectrum with photon index of $\Gamma\sim 2$, a column density of $N_{\rm H}\sim 5\times 10^{20}\,{\rm cm^{-2}}$, and no prominent reflection component. Five years later, *Chandra* captured the source in a heavily-obscured, reflection-dominated state. The observed X-ray spectral variability could be caused by a Compton-thick cloud with $N_{\rm H}\sim 2\times 10^{24}\,{\rm cm^{-2}}$ eclipsing the direct emission of the hot corona, implying an extreme $N_{\rm H}$ variation never before observed in a type-1 QSO. An alternative scenario is a corona that switched off in between the observations. In addition, both explanations require a significant change of the X-ray luminosity prior to the obscuration or fading of the corona and/or a change of the relative geometry of the source/reflector system. Dramatic X-ray spectral variability of this kind could be quite common in type-1 QSOs, considering the relatively few data sets in which such an event could have been identified. Our analysis implies that there may be a population of type-1 QSOs which are Compton-thick in the X-rays when observed at any given time.

Key words: accretion, accretion discs – black hole physics – methods: data analysis – galaxies: active – quasars: general – X-rays: galaxies.

1 INTRODUCTION

Over the last two decades evidence has emerged for variations of the line-of-sight (LOS) column density, ($N_{\rm H}$), in nearby type-2 (obscured) active galactic nuclei (AGN). These are inferred from the shape of the X-ray spectrum, which changes dramatically if a source transitions from a transmission-dominated Compton-thin ($N_{\rm H} < 10^{24} \, {\rm cm}^{-2}$) state to a reflection-dominated Compton-thick (CT; $N_{\rm H} > 10^{24} \, {\rm cm}^{-2}$) one. Sources showing such a behaviour are sometimes referred to as X-ray 'changing look' AGN (Matt, Guainazzi & Maiolino 2003). These variations can be explained if at least part of the circumnuclear absorbing medium in type-2 AGN is clumpy (Risaliti, Elvis & Nicastro 2002; Risaliti 2010;

Bianchi, Maiolino & Risaliti 2012, and references therein), with the spectral changes caused by the transit of a cloud along the line of sight.

In the standard unification picture, the obscuring torus should lie out of the LOS to the nucleus of type-1 AGN, so they are not expected to exhibit this behaviour. The heavily reddened type-1 AGN ESO 323-G77 has none the less displayed $N_{\rm H}$ variations from typical columns of $\sim 10^{23}$ cm⁻² to 1.5×10^{24} cm⁻² (Miniutti et al. 2014). The LOS in this source is suspected to graze the dusty torus, however, so that clumps therein could obscure the central engine, while leaving the broad line region visible. In addition, several cases of CT eclipses have been reported by Risaliti (2010). Furthermore, the archetypical type-1 AGN NGC 5548 shows strong evidence for fast outflows of ionized material that are likely launched from the accretion disc and can block large amounts of the soft X-ray emission (Kaastra et al. 2014).

¹Max Planck Institute for Extraterrestrial Physics, Giessenbachstrasse, Postfach 1312, D-85741 Garching, Germany

²Instituto de Astrofisica, Pontificia Universidad Catolica de Chile, Casilla 306, Santiago 22, Chile

³Excellence Cluster Universe, Boltzmannstr. 2, D-85748, Garching, Germany

⁴Department of Astronomy, University of Illinois at Urbana-Champaign, 1002 W Green Street, Urbana, IL 61801, USA

⁵Argelander-Institut für Astronomie, Auf dem Hügel 71, D-53121 Bonn, Germany

⁶Center for Astrophysics and Space Sciences, Department of Physics, University of California San Diego, 9500 Gilman Drive, La Jolla, CA 92093, USA

⁷Steward Observatory, University of Arizona, 933 N. Cherry Avenue, Tucson, AZ 85721, USA

⁸Department of Astronomy and Astrophysics, The Pennsylvania State University, University Park, PA 16802, USA

⁹Institute for Gravitation and the Cosmos, The Pennsylvania State University, University Park, PA 16802, USA

^{*} E-mail: tsimm@mpe.mpg.de (TS); am@mpe.mpg.de (AM)

Type-1 AGN may also present themselves as Compton-thick in X-rays if there is a strong decrease of the nuclear X-ray luminosity, with a distant reflector, such as the pc-scale dusty torus itself, producing a light echo for some time (Matt et al. 2003). This interpretation has been favoured in the case of the highly variable Seyfert 1 galaxy NGC 4051 (Guainazzi et al. 1998; Uttley et al. 1999) and the Seyfert 1.9 galaxy NGC 2992 (Weaver et al. 1996; Gilli et al. 2000).

The current sample of AGN showing transitions between Compton-thin and -thick states is comprised of bright, local objects for which high-S/N, multi-epoch X-ray observations have been obtained. At the higher redshifts probed by deep X-ray survey fields the situation is complicated by the fact that multiple observations with sufficient S/N are generally not available. Thus, even strong spectral variability of the kind discussed above may remain undetectable. We report here on the discovery of extreme spectral variations of this nature in an otherwise typical broad line type-1 QSO. In the following we assume a Λ CDM cosmology with $H_0 = 70 \, \mathrm{km \, s^{-1} \, Mpc^{-1}}$, $\Omega_{\mathrm{m}} = 0.3$, and $\Omega_{\Lambda} = 0.7$.

2 OBSERVATIONS

The QSO RMID 278 (RA = 214.32112, DEC = +52.29764) is part of the SDSS Reverberation Mapping (SDSS-RM) campaign (Shen et al. 2015). At z = 1.02, it has a black hole mass of $M_{\rm BH} \sim 2.0 \times 10^8 \, \rm M_{\odot}$ (based on single-epoch virial mass estimators), a bolometric luminosity of $L_{\rm bol} \sim 2.8 \times 10^{45} \, \rm erg \, s^{-1}$ (estimated from L_{3000} and mean bolometric correction from Shen et al. 2008), and an Eddington ratio of $\lambda_{\rm Edd} = L_{\rm bol}/L_{\rm Edd} = 0.1$.

RMID 278 was first covered in the X-rays by *XMM-Newton* on 2000 July 20, 21, and 23 with a total exposure of 80 ks (ObsID 0127920401, 0127921001, and 0127921201; see Miyaji & Griffiths 2001), with 247/178 (PN/MOS) net counts detected in the 0.5–8 keV band. About five years later, the source region was covered by *Chandra* with 12 observations, for a total of 189 ks exposure time, taken between 2005 September 13 and 2005 December 11 as part of the *Chandra* AEGIS-X deep survey of the Extended Groth Strip (Laird et al. 2009). The source was detected by *Chandra* with 103 net counts in the 0.5–7 keV band.

3 X-RAY SPECTRAL ANALYSIS

We extracted X-ray spectra of RMID 278 from both *XMM* and *Chandra*. The data reduction of the *XMM* observations and the extraction of X-ray source and background spectra for the PN/MOS detectors was performed following the methodology outlined in Georgakakis and Nandra (2011) and Liu et al. (2016). The individual *Chandra* spectra were extracted and merged into a single spectrum using the ACIS EXTRACT software package (Broos et al. 2010) following Brightman et al. (2014).

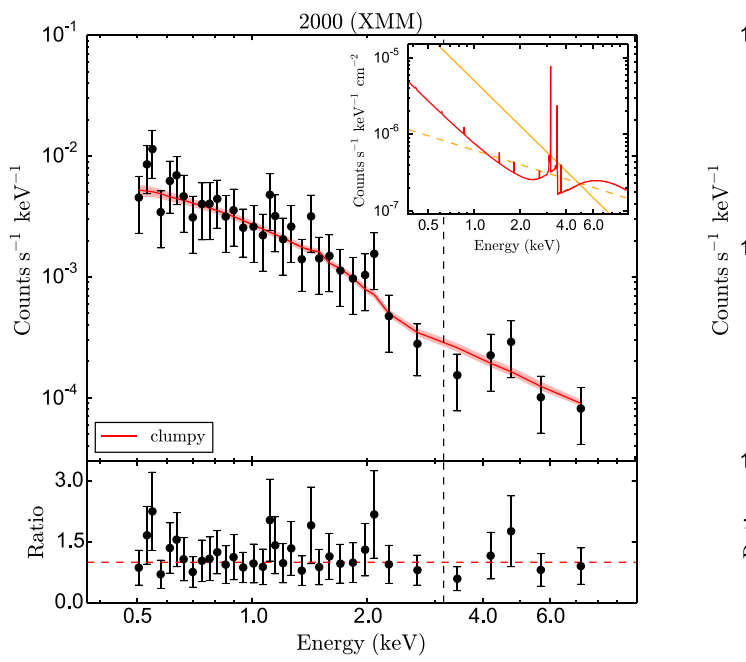
We analysed the X-ray spectra using the Bayesian X-ray Analysis (BXA) software (Buchner et al. 2014). The *XMM* PN/MOS spectra were fitted jointly in the observed-frame 0.5–8 keV band and the EPIC PN/MOS background was modelled following Maggi et al. (2014, see also Liu et al. 2016). The *Chandra* spectrum was fitted in the observed-frame 0.5–7 keV band, applying the background model of Buchner et al. (2014). Spectral models were absorbed by the average Galactic value of $N_{\rm H,gal} = 1.11 \times 10^{20} \, {\rm cm}^{-2}$ (Kalberla et al. 2005) in the direction of the source. Throughout this work, quoted fit parameters and error values correspond to the posterior median and standard deviation, energies are in the source rest-frame, and fluxes, luminosities and column densities are given in cgs units.

The unusual nature of RMID 278 was identified by comparing the photon indices of the subsample of 32 RM-QSOs having both *XMM* and *Chandra* spectra available. The *XMM* spectrum from 2000 is well described by an unabsorbed power law with $\Gamma=1.95\pm0.09$ and small reflection fraction of $\log R=-1.20\pm0.54$ (p1+pex model, see below), typical for a type-1 QSO, with source fluxes of $F_{0.5-2\,\mathrm{keV}}=(9.9\pm1.0)\times10^{-15}$ and $F_{2-10\,\mathrm{keV}}=(1.3\pm0.1)\times10^{-14}\,\mathrm{erg\,cm^{-2}\,s^{-1}}$, respectively. In contrast, the *Chandra* spectrum from 2005 is extremely hard, with $\Gamma=0.62\pm0.24$ and $\log R=-0.64\pm0.76$ for an initial fit assuming a flat Γ -prior. Compared to the *XMM* observation, the soft band flux decreased by a factor of $7.6^{+3.3}_{-2.0}$ (0.5–2 keV, 1σ min/max ranges), while the hard band flux decreased only by a factor of $2.5^{+0.5}_{-0.4}$ (2–10 keV). The two spectra are shown in Fig. 1, which illustrates the strong X-ray spectral variability of RMID 278.

To investigate different physical scenarios for the interpretation of the observed spectral variability, we tested various models for the *Chandra* spectrum of RMID 278. We adopted a Gaussian Γ -prior with mean $\langle \Gamma \rangle = 1.95$ and standard deviation $\sigma = 0.15$, consistent with the observed distribution of the local AGN of Nandra and Pounds (1994); for all other parameters of the models discussed below we assumed uniform or log-uniform priors. The Bayesian model comparison approach outlined in Buchner et al. (2014) relies on the evidence Z of a model: following the scale of Jeffreys (1961), we rule out a model j with 'strong evidence' if the evidence of the model differs by more than a Bayes factor of 10 from the total evidence of all compared models, corresponding to the condition $\log Z_j < \log (\sum_i Z_i) - \log 10$. We compared the following five spectral models:

- (i) A power law with no intrinsic absorption (pl model);
- (ii) An absorbed power law (wabs*pl model);
- (iii) A power law combined with a reflection component, modelled with pexmon (Nandra et al. 2007), i.e. powerlaw+pexmon, (pl+pex model). We define the reflection fraction, R, as the ratio between the normalization of the reflection component and that of the primary power law . The inclination angle of the pexmon model was set to 60° and the photon index linked to that of the primary power law.
- (iv) A warm absorber model cwa18, described in Nandra et al. (2007), to test whether the spectral change can be better explained by the emergence of ionized absorption, potentially associated with outflows from the torus or disc (see e.g. Blustin et al. 2005). The ionization parameter of this model was fitted in the interval $-1 < \log \xi < 3.5$.
- (v) The clumpy torus model (clumpy) of Buchner (2018), which self-consistently models Compton scattering, line fluorescence, and absorption. This model was used to test for the possibility that the spectral change is caused by an eclipse of a dense cloud entering the LOS to the hot corona. The cloud distribution corresponds to a vertical Gaussian with standard deviation σ , consistent with existing clumpy (Nenkova et al. 2008) infrared models. In addition, a covering parameter C is included, describing a CT inner torus ring required to fit local CT AGN. Further parameters are the photon index of the primary power law, the LOS $N_{\rm H}$, and a free viewing angle $\theta_{\rm inc}$. We also add a scattering component (scat) representing Thomson scattering of a volume-filling ionized medium, with a relative normalization to the primary power law (Bianchi, Guainazzi & Chiaberge 2006).

Apart from these five main spectral models, we tested and compared various other spectral models such as an absorbed power law with a scattering but no reflection component



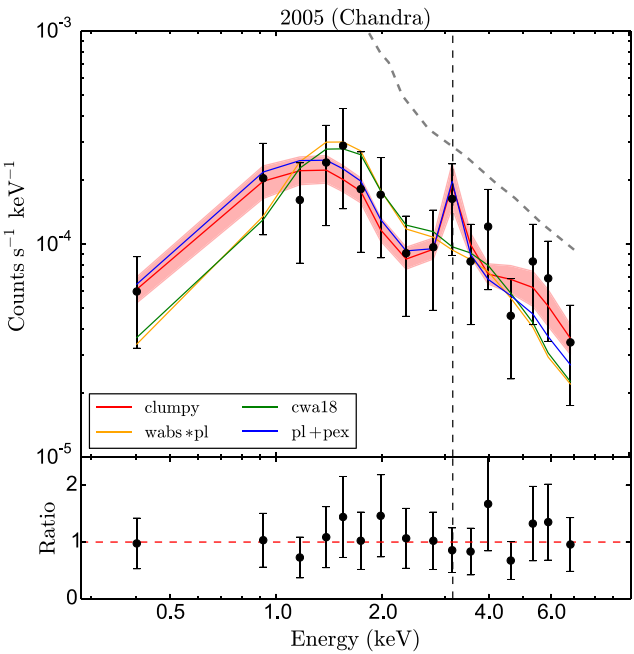


Figure 1. The dramatic X-ray spectral change of the type-1 QSO RMID 278. The XMM EPIC-PN spectrum from 2000 (left-hand panel) is fully consistent with an unobscured power law. In contrast, the Chandra spectrum from 2005 (right-hand panel) is extremely flat. The red curves in both panels display the best-fitting clumpy model together with the 1σ error regions. The ratio of data and model is plotted in the lower panels, and the dashed vertical lines indicate the position of the Fe K α line at the source redshift of z=1.02. The insert in the left-hand panel contains the unfolded spectral models fitted to the XMM spectrum (absorbed power law with $\Gamma \sim 2$, orange curve) and the Chandra spectrum (absorbed power law with $\Gamma \sim 0.6$, orange dashed curve; clumpy model, red curve). Three additional spectral models are shown in the right-hand panel in different colours (see the text for details), along with the clumpy fit to the XMM spectrum (dashed grey line). The observed spectra were grouped to eight counts per bin for visualization only.

Table 1. Fitted model parameters for the *XMM* and *Chandra* spectra of RMID 278. For the former, the torus geometry and *scat* parameters were fixed to the values derived from the latter. The model comparison results ($\Delta \log Z$ with respect to the clumpy model) for the *Chandra* spectrum are shown at the bottom.

Model	XMM		Chandra		
	pl+pex	clumpy	pl+pex	clumpy	
7	1.95 ± 0.09	2.01 ± 0.09	1.75 ± 0.12	1.90 ± 0.14	
$\log N_{ m H}$	_	20.69 ± 0.38	-	24.31 ± 0.57	
$\log R$	-1.20 ± 0.54	_	0.87 ± 0.13	_	
scat	_	-1.29	_	-1.29 ± 0.62	
σ	_	31	_	31 ± 20	
C	_	0.31	_	0.31 ± 0.16	
$\theta_{\rm inc}$	_	55	_	55 ± 20	
$\log L_{ m X}$	43.83 ± 0.03	43.84 ± 0.04	43.13 ± 0.07	44.90 ± 0.41	
Model	clumpy	pl+pex	cwa18	wabs*pl	pl
$\Delta \log Z$	0.00	-0.34	-0.83	-1.41	-1.59
Ruled out	_	_	_	\checkmark	\checkmark

(wabs*pl+scatt), the same model with a reflection component (wabs*pl+pex+scatt), the BNtorus+pex+scatt model of Buchner et al. (2014), and a warm absorber model with reflection and scattering components (cwal8+pex+scatt). These models are discussed in less detail below. The results of the Bayesian model comparison of the five basic models and the fitted parameters of the

¹By choosing the pexmon model we restricted ourselves to an optically thick reflection model, where reflection continuum hump and iron line emission are computed self-consistently. A yet more complex model, in which the line is produced in optically thin material, and thus essentially decoupled from the optically thick reflector, was not considered here for simplicity, given the low signal to noise of our spectrum.

two highest-evidence models are presented in Table 1. We find that the models including a significant reflection component are clearly preferred, with the pl and wabs*pl models ruled out with high significance, whereas the cwal8 model is not formally ruled out by our chosen threshold. The clumpy model has the highest evidence and is fitted with an LOS column density of $\log N_{\rm H} = 24.31 \pm 0.57$, suggesting a CT obscurer. In addition, the clumpy model yields a Γ value that best agrees with the one derived from the XMM spectrum. However, the simpler pl+pex describes the Chandra spectrum almost equally well, albeit with a slightly flatter photon index. Because of the limited number of counts in the Chandra spectrum we could not significantly detect an Fe K α line; however, the 3σ upper limit for the equivalent width is 1 keV, still in agreement with expectations of 0.5–5 keV for a CT LOS (Boorman et al. 2016).

Table 2. Parameters fitted to the Chandra spectrum of RMID 278 for various further spectral models.

Parameter	wabs*pl	cwa18	wabs*pl+scatt	cwa18+pex+scatt	wabs*pl+pex+scatt	BNtorus+pex+scatt
Γ	1.72 ± 0.26	1.80 ± 0.14	1.88 ± 0.14	1.83 ± 0.15	1.81 ± 0.13	1.86 ± 0.14
$\text{Log}N_{\text{H}}$	22.48 ± 0.30	22.67 ± 0.44	24.00 ± 0.51	22.29 ± 0.88	22.18 ± 1.32	24.22 ± 1.11
Log R	_	_	_	0.65 ± 0.69	0.62 ± 0.84	0.05 ± 0.92
$\text{Log }\xi$	_	1.22 ± 1.23	_	0.90 ± 1.14	_	_
scat	_	_	-1.17 ± 0.55	-2.59 ± 1.19	-2.28 ± 1.27	-1.64 ± 0.97
$\text{Log}L_{\text{X}}$	43.56 ± 0.08	43.48 ± 0.06	44.25 ± 0.30	43.21 ± 0.12	43.31 ± 0.48	44.66 ± 0.73

In Fig. 1 (right-hand panel) the fitted models wabs*pl, cwal8, pl+pex, and clumpy are plotted for comparison together with the *Chandra* spectrum.

Adopting the clumpy model as our best model and fixing the torus geometry parameters to the values derived from the *Chandra* spectrum, we find that the *XMM* spectrum is well-fitted by the model with $\Gamma=2.01\pm0.09$ and $\log N_{\rm H}=20.69\pm0.38$, consistent with an unobscured power law. This result implies a dramatic column density variation by a factor of >1000, much larger than the $N_{\rm H}$ variability reported in previous works for both type-1 and type-2 AGN (see e.g. Risaliti et al. 2002; Markowitz, Krumpe & Nikutta 2014). Interestingly, comparing the absorption corrected 2–10 keV power-law luminosities $\log L_{\rm X}=43.84\pm0.04$ (XMM) and $\log L_{\rm X}=44.90\pm0.41$ (*Chandra*), suggests that despite the drop in observed flux the intrinsic luminosity actually increased in the *Chandra* observation by a factor of $11.5^{+20.9}_{-7.4}$.

Considering the second best model, p1+pex, the power-law 2–10 keV luminosity decreased from $\log L_{\rm X} = 43.83 \pm 0.03$ (*XMM*) to $\log L_{\rm X} = 43.13 \pm 0.07$ (*Chandra*), i.e. by a factor of $\sim 5.0^{+1.3}_{-1.0}$. This decrease could indicate a 'switched off' corona. However, the large reflection flux (with $R = 7.4^{+2.6}_{-1.9}$) in 2005, differs substantially from the earlier epoch, with the absolute flux of the reflection component increasing from $F_{2-10\,\mathrm{keV}} = 1.1 \times 10^{-16}$ (*XMM*, 1σ upper value 4.7×10^{-16}) to $F_{2-10\,\mathrm{keV}} = 2.8 \times 10^{-15}$ (*Chandra*, 1σ lower value 2.2×10^{-15}) erg cm⁻² s⁻¹. We tested this explicitly by fitting the XMM spectrum with the pexmon parameters fixed to the same reflection flux as observed by *Chandra*. This is ruled out by both the p1+pex fit with free pexmon parameters ($\Delta \log Z = -2.5$) and the c1 umpy fit to the *XMM* spectrum ($\Delta \log Z = -2.1$).

Comparing the two aforementioned models with the resulting parameters from the wabs*pl, cwa18, wabs*pl+scatt, wabs*pl+pex+scatt, BNtorus+pex+scatt, cwal8+pex+scatt models, we note some important similarities and differences. The fitted parameters of these additionally tested models are presented in Table 2. First of all, none of these models can produce an intrinsic luminosity that is fully consistent with the value derived from the XMM spectrum. There are basically two groups of model solutions. Models with $\log N_{\rm H} < 22.7$ and $\log L_{\rm X} < 43.6$ and models with $\log N_{\rm H} > 24.0$ and $\log L_{\rm X} > 44.2$. This is further demonstrated by Fig. 2, displaying the intrinsic luminosity/column density plane for all tested spectral models. The wabs*pl+scatt exhibits a CT column density and an L_X value that is larger than the XMM one, fully consistent within the errors with the BNtorus+pex+scatt and clumpy model parameters. The models including an ionized absorber have a poorly constrained ionization parameter and L_X values that are lower than the corresponding XMM value. Furthermore, the cwal8+pex+scatt model is fitted with a very low scattering normalization, a low intrinsic luminosity, and a very strong reflection component. In fact, the strong reflection normalization suppresses the ionized absorber part and the soft scattering component, which again

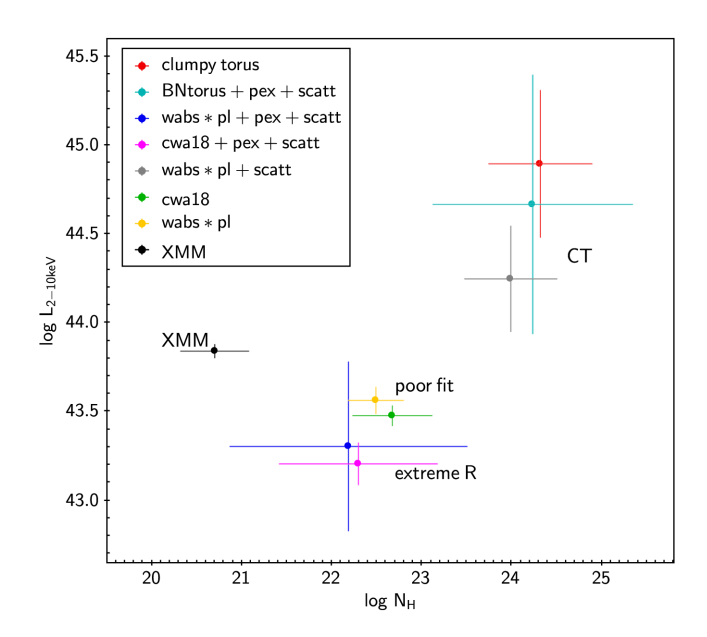


Figure 2. Intrinsic luminosity versus column density for various models (different colours) fitted to the *Chandra* spectrum of RMID 278. The luminosity/column density pair of the clumpy model derived from the *XMM* spectrum is shown as black point for reference. Note that the blue and magenta points correspond to models with $\log R > 0.5$. This provides evidence for a reflection-dominated state, irradiated with intrinsic luminosities of $\sim 10^{44} {\rm erg \ s^{-1}}$, perhaps by a past corona that has now 'switched off'. The models of the yellow and green points have Bayes factors much lower than the clumpy model.

provides evidence for a CT spectral state. We stress that any solution with $\log R > 0$ requires extreme physical scenarios such as light bending, a 'switched off' corona or a CT obscurer. Similarly, the wabs*pl+pex+scatt yields a low scattering normalization, a low intrinsic luminosity, a comparatively low column density, but a very strong reflection component. The BNtorus+pex+scatt model, on the other hand, provides a fit solution that agrees very well with the self-consistent clumpy model. We point out that the Bayesian evidence values of the wabs*pl+pex+scatt, the BNtorus+pex+scatt, and the clumpy models agree within $\Delta \log Z = 0.05$. Therefore, based on the Bayesian factors alone, one could not rule out any of these three models, but all three rule out the simple wabs*pl model and all three models require a strong reflection component and/or large column density increase compared to the XMM spectrum. The Bayesian evidence of the cwal8+pex+scatt model is $\Delta \log Z = 0.15$ higher than for the clumpy model. In this case, the interpretation of the observations would require a significant decrease of the intrinsic luminosity (which is not observed in the optical light curve, see the next section), accompanied by the emergence of an ionized absorber and

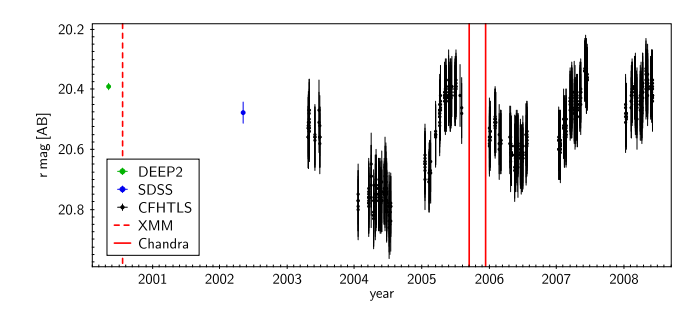


Figure 3. Optical (*r* band) light curve combining observations from the DEEP2 (green), SDSS (blue), and CFHTLS-Deep surveys (black). The dates of the *XMM* and *Chandra* (for the first and last individual pointing) observations are marked by vertical lines.

a strong reflection component, which are both not detected in the *XMM* spectrum. The CT models instead suggest a strong column density and luminosity increase between the two epochs. Both interpretations are challenging to explain within a self-consistent physical scenario.

Summarizing our model comparison analysis, the X-ray data suggest that an eclipse by a dense absorber, or a 'switched off' corona leaving a strong reflection signature, are the most likely scenarios to explain the dramatic spectral variability, though both of them require a large increase in the primary continuum flux prior to and/or during the *Chandra* observation.

4 UV/OPTICAL PROPERTIES OF RMID 278

To investigate the long-term variability of the source further, we collected optical photometry and spectroscopy from various observations closest in time to the X-ray observations. Fig. 3 shows the optical r band (rest-frame $\lambda \sim 3100$ Å) light curve of RMID 278, with data taken from DEEP2 imaging (Coil et al. 2004), the SDSS-DR12 catalogue (Alam et al. 2015), and the CFHTLS-Deep survey (processed with the CFHTLenS pipeline; see Erben et al. 2013). The observed optical variability in the interval between the XMM and Chandra observations corresponds to a maximum change in flux by a factor of \sim 1.5, consistent with typical QSO variability (e.g. Simm et al. 2016). This is much less than the variability in optically selected changing look AGN (e.g. LaMassa et al. 2015; MacLeod et al. 2016), and there is no hint of a large (factor \sim 10) continuum change implied by our X-ray spectral modelling. Of course, if the source underwent a heavily absorbed (Compton Thick) flare from the very innermost part of the disc/corona between 2000 and 2005, this might have been invisible in the optical band, whose light is generated by the outer accretion disc. We note that the intrinsic X/O ratio at the time of the XMM and Chandra epochs is unknown, since optical data are only available several months before and after the X-ray observations. None the less, assuming that the optical flux is similar to the flux observed closest to the X-ray observations, we obtain X/O(XMM) = -0.2 and X/O(Chandra) = -0.9, using the 0.5-2 keV flux and the *i* band optical flux. If we instead assume an intrinsic flux increase by a factor of 10 for the Chandra spectrum, then X/O(Chandra) = 0.8, again assuming the optical flux stayed the same. These values are all typical and within the expected locus for AGN of X/O = ± 1 (see e.g. Civano et al. 2012). Still, in the case of a CT obscurer, the actual values of the X/O ratios at both epochs depend strongly on the location of the obscurer, which is not determined from our data.

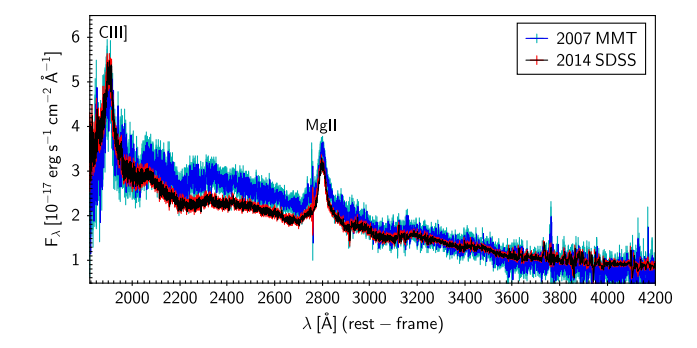


Figure 4. Comparison of the 2007 MMT (blue, 1σ errors in cyan) and the 2014 SDSS-RM spectrum (black, 1σ errors in red).

No optical spectra are available between 2000 and 2005, but the source was observed on 2007 March 16 with the MMT/Hectospec spectrograph (Coil et al. 2009) and has CFHT photometry with $r=20.45\pm0.10$ measured just one day later. The MMT spectrum is shown together with the 2014 SDSS-RM spectrum (co-add of 32 spectra taken over a period of 6 month, Blanton et al. 2017) in Fig. 4. Both spectra display prominent broad MgII $\lambda\lambda$ 2798 Å and CIII] $\lambda\lambda$ 1909 Å emission lines and a strong blue continuum. No wind signatures, such as blueshifted absorption or reddening, are apparent.

Thus, the optical light curve and the spectra disfavour a strong variation of the total accretion luminosity or any substantial optical obscuration as well as a change of the optical AGN type, unless these occurred during the periods not covered by the observations.

5 DISCUSSION AND CONCLUSIONS

The repeat X-ray spectra of RMID 278 provide strong evidence for this typical $z\sim 1$ type-1 QSO switching from a transmission-dominated to a reflection-dominated state. This dramatic spectral change may be caused by either a nuclear eclipse event or a strong decrease of the corona luminosity, leaving the reflected emission from distant material as the dominant component of the source spectrum. In addition, the strong reflection component detected by *Chandra* but not by *XMM*, requires a significant increase of the primary continuum X-ray flux in both scenarios, or a dramatic change in the source geometry. This is further supported by the relatively small decrease of the observed 2–10 keV flux in between the two epochs.

In the 'switched off' corona scenario, the X-ray reflection most likely comes from distant material, such as the pc-scale dusty torus. Its location can be estimated from the dust sublimation radius. Given the bolometric luminosity of our source, we obtain $R_{\text{sub}} \sim$ 0.25-0.69 pc adopting either the relation fitted to observed K band time lags (Suganuma et al. 2006) or the theoretical prediction of Barvainis (1987). Based on these rough estimates, we would expect to still see a notable reflection echo in the 2005 spectrum, if the central engine switched off sometime between 2001 and 2005. On the other hand the strong increase in the reflection component between 2000 and 2005 would require a sustained and significant increase in the coronal luminosity prior to fading away, or a major change of the geometry of the reflector with respect to the corona in between the observations. The optical light curve (Fig. 3) displays no extreme variability between the X-ray observations, which, together with the optical spectra (Fig. 4), implies that the source probably did not undergo major changes in accretion rate or change its (optical) AGN type during this period. Even though AGN variability can be much more extreme in X-rays than in optical, especially on short time-scales (Uttley & Casella 2014), these arguments tend to disfavour the 'switched off' corona.

The alternative hypothesis is that the source is in an X-ray bright, heavily obscured state at the time of the Chandra observations. Within the best-fitting clumpy model interpretation, the event is most probably caused by a dense cloud eclipsing the Xray corona, resulting in an $N_{\rm H}$ variation from the completely unobscured regime of $N_{\rm H} \sim 5 \times 10^{20} \, {\rm cm}^{-2}$ to the CT regime with $N_{\rm H} \sim 2 \times 10^{24} \, {\rm cm}^{-2}$. To the best of our knowledge, such an extreme $N_{\rm H}$ variation by more than three orders of magnitude has never before been observed in a type-1 QSO. This scenario also requires a large increase in the X-ray luminosity at the time of the Chandra observation. Rather than being a coincidence, it could be that these events are connected. The increase in intrinsic luminosity implied by the X-ray spectrum could bring RMID 278 close to or perhaps even beyond the Eddington limit. Such a luminosity increase could launch a wind of CT clouds, which in turn obscures the hot corona (see e.g. Pier & Krolik 1992). However, the available data suggest that this would have been a dramatic and short (time-scale few months) 'outburst', possibly resulting in a 'failed wind' that lifted CT material for only a short period of time. Due to the large uncertainties of the intrinsic luminosity in the CT solution, the implied luminosity increase should not be overinterpreted though. In any case, irrespective of the favoured interpretation of the observations, the data strongly suggest a dramatic change in the spectral properties of the source, associated to a significant change in the absorber column density, possibly accompanied by further changes in the source luminosity and/or relative geometry of the source/reflector system.

How often could these events occur? Based on a statistical analysis of X-ray eclipse events in local Seyfert galaxies monitored with RXTE, Markowitz et al. (2014) estimated the probability for a type-1 AGN to undergo an X-ray eclipse to be 0.6 per cent 16.6 per cent . They did not detect any CT obscuration in their type-1 AGN sample (c.f. Miniutti et al. 2014) inferring an upper limit of < 15.8 per cent for such events. The CT obscuration in RMID 278 was seen for one out of 32 type-1 RM-QSOs with repeat XMM and Chandra spectra. Given this limited data set, we are unable to derive robust constraints on the fraction of the type-1 QSOs undergoing CT eclipses. However, considering that we obtained spectra at just two epochs, and over a single time baseline of \sim 5 yr, this behaviour could be very common. Comparing with the non-detections of Markowitz et al. (2014) and Torricelli-Ciamponi et al. (2014) in nearby type-1 AGN, this could imply an important difference in the obscuration properties of local AGN and the more typical accreting SMBH found in deep X-ray surveys. Large area surveys with spectral timing information are needed to unveil the intrinsic fraction of CT obscuration events among the AGN population. The future surveys performed by SRG/eROSITA (Merloni et al. 2012) will provide an unprecedentedly large sample of type-1 AGN with repeated Xray observations on various time-scales, allowing for a thorough statistical study of these extreme variations.

ACKNOWLEDGEMENTS

JB acknowledges support from FONDECYT Postdoctorados grant 3160439 and the DFG cluster of excellence 'Origin and Structure of the Universe'. This research used the facilities of the Canadian Astronomy Data Centre operated by the National Research Council of Canada with the support of the Canadian Space Agency.

REFERENCES

Alam S. et al., 2015, ApJS, 219, 12

Barvainis R., 1987, ApJ, 320, 537

Bianchi S., Guainazzi M., Chiaberge M., 2006, A&A, 448, 499

Bianchi S., Maiolino R., Risaliti G., 2012, Adv. Astron., 2012, 782030

Blanton M. R. et al., 2017, AJ, 154, 28

Blustin A. J., Page M. J., Fuerst S. V., Branduardi-Raymont G., Ashton C. E., 2005, A&A, 431, 111

Boorman P. G. et al., 2016, ApJ, 833, 245

Brightman M., Nandra K., Salvato M., Hsu L.-T., Aird J., Rangel C., 2014, MNRAS, 443, 1999

Broos P. S., Townsley L. K., Feigelson E. D., Getman K. V., Bauer F. E., Garmire G. P., 2010, ApJ, 714, 1582

Buchner J., 2018, Unified Clumpy AGN Torus Model and X-ray spectrum

Buchner J. et al., 2014, A&A, 564, A125

Civano F. et al., 2012, ApJS, 201, 30

Coil A. L., Newman J. A., Kaiser N., Davis M., Ma C.-P., Kocevski D. D., Koo D. C., 2004, ApJ, 617, 765

Coil A. L. et al., 2009, ApJ, 701, 1484

Erben T. et al., 2013, MNRAS, 433, 2545

Georgakakis A., Nandra K., 2011, MNRAS, 414, 992

Gilli R., Maiolino R., Marconi A., Risaliti G., Dadina M., Weaver K. A., Colbert E. J. M., 2000, A&A, 355, 485

Guainazzi M. et al., 1998, MNRAS, 301, L1

Jeffreys H., 1961, Theory of Probability, 3rd. Clarendon Press, Oxford

Kaastra J. S. et al., 2014, Science, 345, 64

Kalberla P. M. W., Burton W. B., Hartmann D., Arnal E. M., Bajaja E., Morras R., Pöppel W. G. L., 2005, A&A, 440, 775

Laird E. S. et al., 2009, ApJS, 180, 102

LaMassa S. M. et al., 2015, ApJ, 800, 144

Liu Z. et al., 2016, MNRAS, 459, 1602

MacLeod C. L. et al., 2016, MNRAS, 457, 389

Maggi P. et al., 2014, A&A, 561, A76

Markowitz A. G., Krumpe M., Nikutta R., 2014, MNRAS, 439, 1403

Matt G., Guainazzi M., Maiolino R., 2003, MNRAS, 342, 422

Merloni A. et al., 2012, preprint (arXiv:1209.3114)

Miniutti G. et al., 2014, MNRAS, 437, 1776

Miyaji T., Griffiths R. E., 2001, in Neumann D. M., Van J. T. T., eds, Clusters of galaxies and the high redshift universe observed in X-rays. Savoie, France

Nandra K., Pounds K. A., 1994, MNRAS, 268, 405

Nandra K., O'Neill P. M., George I. M., Reeves J. N., 2007, MNRAS, 382, 194

Nenkova M., Sirocky M. M., Nikutta R., Ivezić Ž., Elitzur M., 2008, ApJ, 685, 160

Pier E. A., Krolik J. H., 1992, ApJ, 399, L23

Risaliti G., 2010, in Peterson B. M., Somerville R. S., Storchi-Bergmann T., eds, Co-Evolution of Central Black Holes and Galaxies. Proc. IAU Symposium 267, 299

Risaliti G., Elvis M., Nicastro F., 2002, ApJ, 571, 234

Shen Y., Greene J. E., Strauss M. A., Richards G. T., Schneider D. P., 2008, ApJ, 680, 169

Shen Y. et al., 2015, ApJS, 216, 4

Simm T., Salvato M., Saglia R., Ponti G., Lanzuisi G., Trakhtenbrot B., Nandra K., Bender R., 2016, A&A, 585, A129

Suganuma M. et al., 2006, ApJ, 639, 46

Torricelli-Ciamponi G., Pietrini P., Risaliti G., Salvati M., 2014, MNRAS, 442, 2116

Uttley P., Casella P., 2014, Space Sci. Rev., 183, 453

Uttley P., McHardy I. M., Papadakis I. E., Guainazzi M., Fruscione A., 1999, MNRAS, 307, L6

Weaver K. A., Nousek J., Yaqoob T., Mushotzky R. F., Makino F., Otani C., 1996, ApJ, 458, 160

This paper has been typeset from a TEX/IATEX file prepared by the author.